Matter

Article

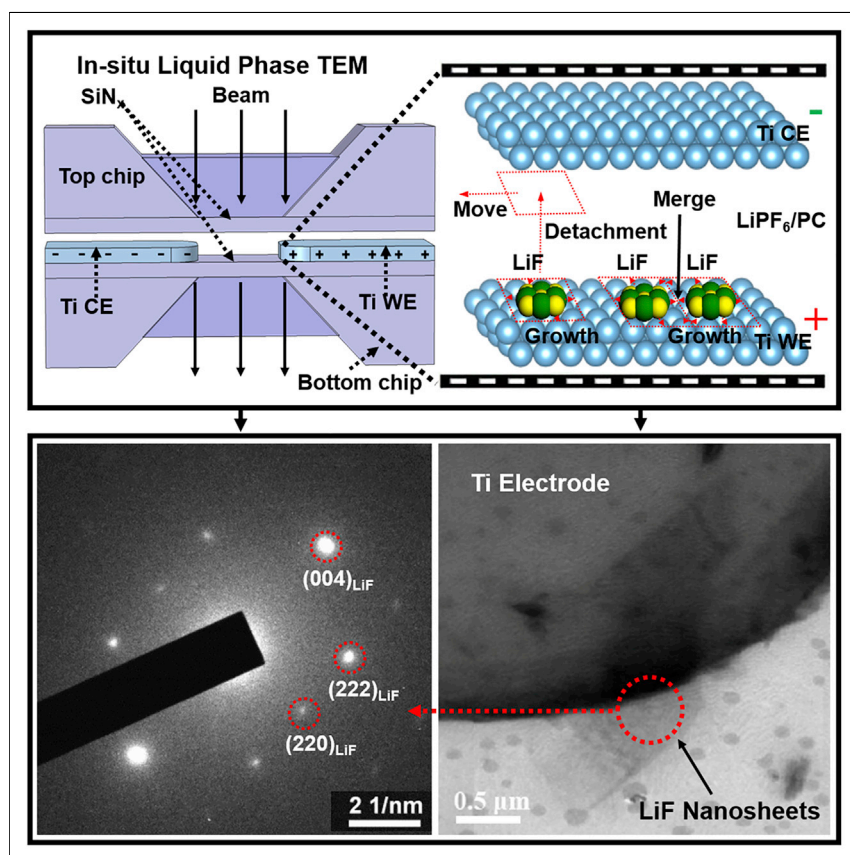# *In situ* TEM visualization of LiF nanosheet formation on the cathode-electrolyte interphase (CEI) in liquid-electrolyte lithium-ion batteries

Qingyong Zhang, Jiale Ma, Liang Mei, Jun Liu, Zhenyu Li, Ju Li, Zhiyuan Zeng

zhiyzeng@cityu.edu.hk (Z.Z.)
liju@mit.edu (J.L.)
zyli@ustc.edu.cn (Z.L.)

Highlights

In situ liquid cell TEM reveals that LiF grows on positively charged Ti electrodes

Structure of *in situ*-formed LiF is confirmed by selected area diffraction pattern

Nucleation, growth, merging, detachment, and movement behaviors of LiF are observed

Theoretical modeling indicates two reaction paths for LiF formation on Ti electrode

Discovery
A new material or phenomena

Matter

CellPress

Article

In situ TEM visualization of LiF nanosheet formation on the cathode-electrolyte interphase (CEI) in liquid-electrolyte lithium-ion batteries

Qingyong Zhang,[1,6] Jiale Ma,[3,6] Liang Mei,[1] Jun Liu,[4] Zhenyu Li,[3,*] Ju Li,[5,*] and Zhiyuan Zeng[1,2,7,*]

SUMMARY

The formation behaviors of LiF nanocrystals have been studied on anodes in Li-ion batteries; there is no research work reporting LiF crystal growth on cathodes. Here, we report a real-time LiF crystal formation on positively charged titanium (Ti) electrodes in an electrochemical liquid cell with 150-nm-thick Li hexafluorophosphate ($LiPF_6$)/propylene carbonate (PC) liquid electrolyte loaded. The LiF nanocrystals show two-dimensional (2D) morphologies on the electrode surface, which can serve as a cathode electrolyte interface (CEI). Furthermore, the merging of LiF nanosheets was also observed, which may underlie the self-healing ability of LiF-based CEIs. Theoretical modeling indicates that there are two types of LiF formation paths on positive voltage-biased Ti electrodes. This work shows the remarkable morphing mobility and self-healing ability of LiF nanosheets and sheds light on strategies of modulating LiF nanocrystals and cathode surface chemistry for improving battery performance and cycle life.

INTRODUCTION

Li-ion batteries are key energy storage devices. However, safety concerns[1] and short lifespan[2] induced by Li dendrite formation and exfoliation of anode materials[3,4] limit their application. Solid electrolyte interphase (SEI) can block electrons, allow Li ions to pass through, and suppress Li dendrite growth, which is critical for sustaining high performance. Thus far, extensive research processes on anode SEI have achieved profound development and understanding.[5–7] SEI usually forms at the first several cycles on anodes via the reduction of solvent in the electrolyte,[8] and its structure and chemistry actively evolve in the ensuing charge/discharge cycles.[9,10] It was proposed that SEI contains a compact inorganic inner layer with low resistance and porous organic outer layer with high resistance,[11,12] and the compact inorganic layer is composed of Li_2O, LiH, and LiF.[13–15] The inner SEI inorganic layer is generated because negatively charged electrodes repel anions from the inner layer.[16] LiF-rich SEI improves the rate capability of anodes due to the fast diffusion of Li^+ through the SEI layer and the thermodynamic stability of LiF on both ends of the voltage window.[17] In addition, LiF plays an important role in the cyclability of the anode. For example, fluorinated SEI can regulate the Li deposition and enhance the stability and safety of the anode,[18] and the LiF-organic bilayer interphase improves the cycling performance of batteries that contain micro-sized Si, Al, and Bi anodes and commercial $LiFePO_4$ and $LiNi_{0.8}Co_{0.15}Al_{0.05}O_2$ cathodes.[19] Zhang et al. reported that LiF acts as artificial SEI that can prolong the cycle life of the $Li_4Ti_5O_{12}$ (LTO) electrode via the LiF film separating electrolytes from LTO and suppressing the decomposition of $LiPF_6$.[20] The SEI-functionalized membrane derived from the

Progress and potential

For Li-ion battery cathodes, the electrochemical reaction between electrode and electrolyte can consume electrolytes and promote LiF nanocrystal formation on the cathode surface. LiF separates cathodes from electrolytes, which is beneficial to battery performance. However, limited characterization techniques hinder the mapping out of dynamic deposition behaviors of LiF crystals during cathode reactions; this has long bedeviled the battery field. We captured the dynamic deposition behaviors of LiF nanocrystals on positively charged Ti electrodes via *in situ* liquid cell TEM, and we identified the structure of the LiF nanocrystals by selected area electron diffraction patterns. We also observed the merging, detachment, and movement of LiF nanocrystals, which show a remarkable morphing mobility and self-healing ability of LiF nanocrystals. Our results deepen the understanding of LiF nanocrystal formation on cathodes and provide guidance to modulating LiF nanocrystals for improving cathode performance.

CellPress

LiF-decorated layered carbon structure can hinder electron transfer and thus avoid Li deposition.[21]

In fact, in $LiPF_6$ containing electrolytes, LiF is not only present in SEI on the anode side, but also exists in the cathode electrolyte interphase (CEI) on the cathode side.[22,23] For instance, LiF was detected on the $LiNiO_2$ electrode upon immersion in electrolytes of 1 M $LiPF_6$ in ethylene carbonate (EC):dimethyl carbonate (DMC) (1:1).[24] Using the same electrolyte, the CEI composition on $LiCoO_2$ comprising O–C=O, Li_2CO_3, $Li_xPF_yO_z$, and LiF, and the composition remains unchanged after the first cycle.[25] With electrolyte 1.3 M $LiPF_6$ in EC/ethyl methyl carbonate (EMC)/di-ethyl carbonate (DEC) = 3/2/5 (v/v) used, on the $LiNi_{0.5}Mn_{1.5}O_4$ surface, $Li_xPF_yO_z$, $PF_x(OH)_y$, and LiF were detected when the cell was charged to 4.2, 4.7, and 4.9 V.[26] In electrolyte of 1 M $LiPF_6$ + EC:DMC (1:1), Li_2CO_3, Li_xPF_y, P-O, P-F, and LiF were detected on the surface of $LiNi_{0.8}Co_{0.15}Al_{0.05}O_2$ after being charged to 3.6, 4.0, and 4.75 V.[27] In electrolyte of 1 M $LiPF_6$ in EC:EMC (4:6 by weight), after being cycled for 200 cycles, the CEI composition on $LiNi_{0.76}Mn_{0.14}Co_{0.1}O_2$ contained RCO_3Li, Li_2CO_3, $Li_xPF_yO_z$, Li-B-O, and LiF.[28] LiF in CEI may play an important role in the electrochemical performance and cycle life of the cathode material. For example, a LiF-coated $LiNi_{0.8}Co_{0.1}Mn_{0.1}O_2$ cathode can enhance high-temperature performance and improve rate capability.[29] LiF-modified $LiNi_{1/3}Co_{1/3}Mn_{1/3}O_2$ has shown better low-temperature performance and rate capability than unmodified $LiNi_{1/3}Co_{1/3}Mn_{1/3}O_2$. Because LiF may decrease the dissolution of metal ions, the conductivity of the surface layer is enhanced through partial F-substitution.[30]

Given the importance of LiF, the formation mechanism of LiF was of interest. Two types of electrochemical reactions were attributed to the formation of LiF. One is the reduction of $LiPF_6$ on anodes[31,32] at a potential range of 0.4–0.6 V vs Li/Li^+, which results in the formation of LiF and Li_xPF_y.[31,33,34] Another is the oxidation of solvent[35,36] on the cathode, and the oxidation potential varies with different electrodes. For commonly used solvents such as propylene carbonate (PC) and EC, the oxidation reaction is a ring-opening reaction,[37–41] but the reaction path is not clear. Hence, numerous *ex situ* and *in situ* analytical tools were used to characterize the generated LiF crystals. The *ex situ* characterization techniques include X-ray photoelectron spectroscopy (XPS),[17,24,42–44] double-resonance solid-state NMR spectroscopy,[45] time-of-flight secondary ion mass spectrometry (ToF-SIMS),[46] transmission electron microscopy (TEM),[7,23] and cryo-scanning TEM (STEM).[47] However, due to the water and air sensitivities of the sample, some structural changes occur during the *ex situ* characterization processes, which is why *in situ* characterization techniques such as non-destructive analysis tools are widely used to capture dynamic electrode reactions in Li-ion batteries during the charge/discharge process.[7,48–51] The majority of reports focused on SEI,[52–54] and few reports were focused on LiF. It is still unclear why LiF can form on the cathode side, and *in situ* studies of LiF electrodeposition have not been achieved thus far.

Here, we report a real-time LiF formation on positively charged titanium (Ti) electrodes in $LiPF_6$/PC electrolytes via *in situ* TEM by using an electrochemical liquid cell with 90-nm-thick patterned Ti electrodes as the working electrode (WE) and the counter electrode (CE). Note that while typically, people use Cu and Al as the current collectors or electrodes in Li-ion batteries, we use Ti as the WE because the liquid cell nanofabrication process cannot successfully pattern Cu and Al electrodes with good conductivity on the Si substrate. This may be because the adhesion between Cu (Al) and Si substrate is not good or because the patterned Cu (Al) electrodes are too thin (90 nm) and too easily oxidized. Our *in situ* experiments

[1]Department of Materials Science and Engineering, City University of Hong Kong, 83 Tat Chee Avenue, Kowloon, Hong Kong 999077, P.R. China

[2]Shenzhen Research Institute, City University of Hong Kong, Shenzhen 518057, P.R. China

[3]Hefei National Laboratory for Physical Sciences at the Microscale, University of Science and Technology of China, Hefei, Anhui 230026, P.R. China

[4]School of Materials Science and Engineering and Guangdong Provincial Key Laboratory of Advanced Energy Storage Materials, South China University of Technology, Guangzhou 510641, Guangdong, P.R. China

[5]Department of Nuclear Science and Engineering and Department of Materials Science and Engineering, Massachusetts Institute of Technology, Cambridge, MA 02139, USA

[6]These authors contributed equally

[7]Lead contact

*Correspondence: zhiyzeng@cityu.edu.hk (Z.Z.), liju@mit.edu (J.L.), zyli@ustc.edu.cn (Z.L.)

https://doi.org/10.1016/j.matt.2022.01.015
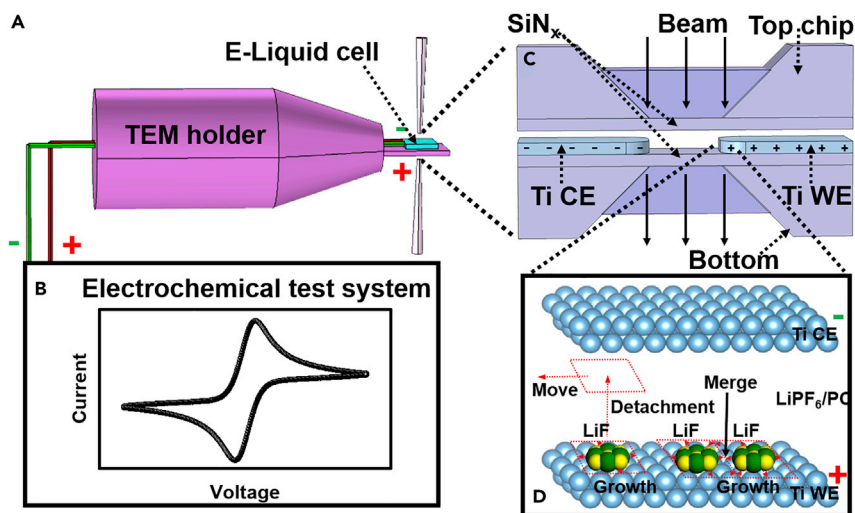
Matter
Article

CellPress

Figure 1. A schematic of the experimental setup for the *in situ* TEM study of LiF electrochemical deposition

(A) A customized electrochemical TEM sample stage.

(B) An electrochemical program is applied to the electrochemical cell using an electrochemical workstation.

(C) An electrochemical liquid cell that fits the sample stage in (A).

(D) *In situ* deposition of LiF nanosheet on positively charged Ti electrodes; some are detached from the Ti electrode.

combined with density functional theory (DFT) calculations allow for an in-depth understanding of LiF growth behavior on positively charged electrodes.

RESULTS AND DISCUSSION

Nucleation, growth, dissolution, and characterization of LiF nanocrystals

Figure 1 is a schematic illustration showing the real-time monitoring of the electrochemical reaction using an electrochemical liquid cell after the loading of the Li-ion battery electrolyte (1 M $LiPF_6$ dissolved in PC) in a liquid cell. The sealed liquid cell was mounted onto the self-designed TEM holder. With electrochemical testing program cyclic voltammetry (CV) applied on pattern Ti electrodes (as shown in Figure 1B) through the connecting wires that were embedded in the TEM holder, LiF nucleation and growth behaviors were captured on the Ti WE in the SiN_x window area as revealed by *in situ* TEM (as shown in Figure 1C). Here, we traced LiF formation during CV measurement, with cell voltages ranging from 4 to −4 V versus pseudo-reference electrode Ti (PSE Ti) at a scan rate of 100 mV/s (as shown in Figure S1). Due to the limited space inside the liquid cell, there was no Li-metal reference electrode, and thus the CE also worked as the reference electrode.

Figures 2A–2F show the sequential images that reveal the evolution of LiF nanocrystals nucleated on the Ti electrode under CV, which were captured by *in situ* TEM (also see Video S1). The WE was cycled between 4 and −4 V (versus PSE Ti). Figures 2G–2L are the simulated three-dimensional (3D) LiF crystals corresponding to Figures 2A–2F, which clearly show the nucleation, growth, tilting, and dissolution of LiF nanocrystals. Here, cell potential cannot reflect the real state of the WE since the reference electrode is absent, but the state of WE can be determined by the current. Figure 2M shows the corresponding applied electrical potential and measured electric current from frame A to frame F. Figure 2N is the measured area of the deposited LiF crystal that projected on the plane of the Ti electrode and the SiN_x membrane
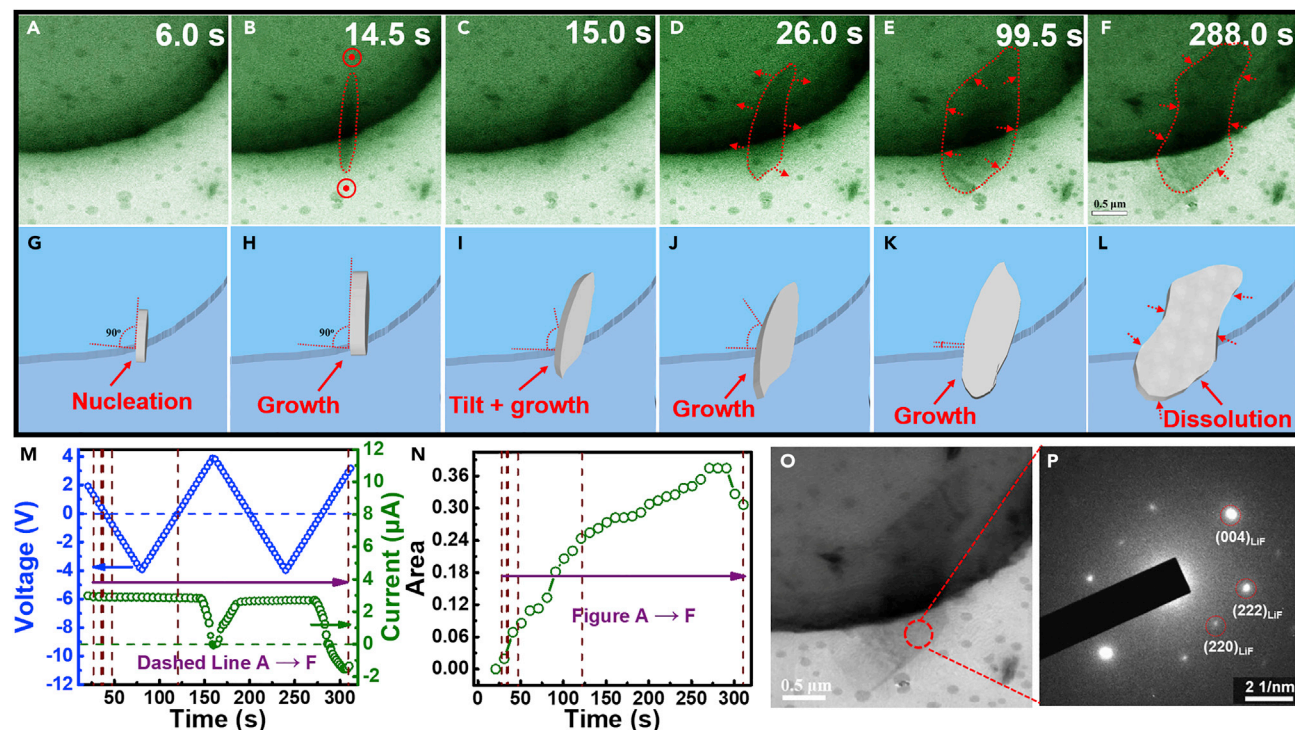
Figure 2. Morphology evolution of LiF crystal on Ti electrode and its crystal structure identification

(A–F) Time series of TEM images illustrate the formation of LiF nanosheet on positively charged Ti electrodes.

(G–L) 3D images corresponding to (A)–(F) display the behavior of nanosheet clearly.

(M) Corresponding voltage loaded on the electrochemical liquid cell and measured current from electrochemical workstation.

(N) The projected area of LiF nanosheet as a function of time during cyclic voltammetry in the voltage range of 4 to −4 V at a scan rate of 100 mV/s.

(O) TEM image of the *in situ*-formed LiF nanosheet in the liquid cell.

(P) The selected area electron diffraction (SAED) pattern of the nanosheet collected in the red dashed circle area in (O).

(perpendicular to the electron beam direction). The intersections of vertical dashed lines with the voltage-current curve and area curve in Figures 2M and 2N are the specific potential, current, and area that correspond to Figures 2A–2F. As a side note, in Figure 2A, there are some dark spots on the observed electrode. The dark spots on the Ti electrode are from residual photoresists during the E-cell fabrication process instead of electrolyte decomposition deposits, since they were observed at the beginning of the *in situ* TEM test, as shown in Video S1 (see also Figure S2A). Most dark spots on the Ti electrode remain unchanged during the *in situ* TEM test, as shown in Figures 2A–2F, which confirms that the dark spots were not from electrolyte electrochemical decomposition. However, a few dark spots changed during the *in situ* TEM observation process, as highlighted in Figure S3 with red circles. This may originate from some side reactions between the residual photoresist and electrolyte under the electron beams. From Figures 2A and 2B, the voltage of WE (versus PSE Ti) varies from 1.32 to 0.47 V, and there is a deposit nucleating on the electrode (also see Figures 2G and 2H). Then, from Figures 2B to 2D, the corresponding voltages of WE (versus PSE Ti) are 0.47, 0.42, and −0.68 V, respectively, and the LiF nanosheet grows in the vertical direction (perpendicular to Ti electrode plane and SiN$_x$ window plane, as shown in red concentric circles in Figure 2B; also see Figure 2H) at the beginning. The nanosheet quickly touches the top chip of the liquid cell on the SiN$_x$ window due to the limited internal space (150 nm) of the liquid cell in the thickness direction. In this case, the nanosheet tilts and slides from the vertical direction to the horizontal direction to accommodate the fast

Matter
Article

CellPress

increasing dimensions of the grown nanocrystal (see Figures 2D and 2J). Figures 2D and 2E show that the nanosheet grows gradually as the voltage of WE (versus PSE Ti) changes from −0.68 to 0.03 V, and red arrows in Figures 2D and 2E indicate the horizontal growth direction. The projected area of the nanocrystal becomes increasingly larger during this period, as shown in Figure 2N. According to Figure 2M, the measured current corresponding to Figures 2A–2E is positive (anodic current), which means that the WE is positively charged. Thus, deposit forms on the positively charged Ti electrode.

From Figure 2F (also Figure 2L), we found that at ∼288 s, the measured current changes to negative for the second time. In the meantime, the nanosheet seems to dissolve. For Video S1, the video began at ∼20 s after the beginning of the CV test, so for the second time that the current changes from positive to negative (288 s), the corresponding time in Video S1 should be 268 s. To double confirm the dissolution process of the LiF nanosheet, the area change of the LiF nanosheet on the horizontal plane during a period of 268–288 s in Video S1 was extracted and analyzed as shown in Figure S4. It indicates that the LiF nanocrystal did dissolve under negative current. Actually, at 167 s, the current changes from positive to negative for the first time as shown in Figure 2M; this negative current remains for a very short time and it does not lead to a decreasing trend of the area but just a plateau, as shown in Figure 2N.

To further confirm that the in situ-formed nanosheet is LiF crystal, we stopped the electrochemical reaction and dried the liquid cell in the glove box. Then, we loaded it into TEM for final morphology and crystal structure identification. As shown in Figures 2O and 2P, the LiF morphology in Figure 2O is consistent with the final morphology in the video. The lateral size is approximately hundreds of nanometers (also see the magnified TEM of the LiF crystal shown in Figure S5). The selected area electron diffraction (SAED) pattern (in Figure 2P) of the nanosheet shows a face-centered cubic structure with lattice spacings of 1.4240, 1.1625, and 1.0068 Å, which are assigned to the $(220)_{LiF}$, $(222)_{LiF}$, and $(004)_{LiF}$ planes, respectively. Based on the identified planes, the zone axis of this deposited LiF nanocrystal is [$\bar{1}$10]; this is the first direct evidence that the LiF nanocrystal can form in situ on the positively charged Ti electrode. To exclude the electron beam effect on the LiF deposition during the in situ TEM movie capturing process, we have also created a control experiment in a liquid cell under CV test without the TEM recording process. Then, we stopped the electrochemical reaction and dried the liquid cell in a glove box and loaded the electrochemical liquid cell into TEM for final morphology checking. We still saw the LiF nanosheets on the Ti electrode, as shown in the TEM image and SAED image in Figure S6A, and also the magnified TEM in Figure S6B (with marked red circle indicating the SAED collecting area). Hence, the electron beam effect during the in situ TEM capturing process for the formation of LiF crystals can be excluded.

There is no full surface coverage by any CEI layer, whether amorphous or crystalline, but only partial coverage by LiF. SEI mainly formed on the anode or Li-metal during the first few charge/discharge cycles, especially in the discharge process—that is, during the reduction process.[13,55,56] Note that the electrochemical reaction in the Li-ion battery electrolyte on the Ti electrode without intercalation provides an opportunity to capture the LiF nanosheet on the surface of the Ti electrode. As shown in Figures S7B and S7E, the potential of Ti CE versus Li/Li$^+$ changes dramatically when current flows through the electrode. The potential of the cells used in our experiment represents the difference between the potential of WE (U_{WE}) and the potential of CE (U_{CE}). Thus, the cell potential cannot reflect the exact U_{WE}, which is

⮐ CellPress

Matter
Article

based on the comparison of CV curves (as shown in Figures S7A, S7C, S7D, and S7F), which means that the applied cell voltage cannot indicate whether oxidation or reduction reaction occurs on the WE. In other words, without a reference electrode applied in the tiny liquid cell, the cell voltage cannot indicate whether the electrode is positively charged or negatively charged. Hence, in the self-designed electrochemical liquid cell, we used the current measured in the electrode as the indicator of the electrode state. Figure S8 shows how to determine the oxidation/reduction state of the WE based on current. When the current is positive (anodic), the electrode is positively charged and an oxidation reaction occurs on the electrode. Otherwise, the electrode is negatively charged and a reduction reaction (cathodic current) occurs on the electrode. It is noteworthy that the CV curves in Figures S7A–S7C are discontinuous. This is because we start the CV tests from the open circuit potential (OCP) and scan for only one cycle, so the discontinuity is inevitable.

Although we have accomplished the real-time imaging of electrochemical reactions in commercial electrolyte $LiPF_6$/PC for Li-ion batteries using TEM, there are still drawbacks in the setup. For instance, since a Li-ion source electrode was lacking inside the liquid cell to supply the consumed Li ions during reactions, it is expected that the concentration of Li ions in the electrolyte changes during the reaction. The total Li consumption in the electrolyte has been estimated.[50] However, such changes do not drastically affect the deposition kinetics. We have observed LiF deposition on the positively charged Ti electrode, and the observed LiF formation was doubly confirmed by *ex situ* liquid cell experiments. Furthermore, we have also conducted *ex situ* experiments by using the commercial cathode material $LiNi_{0.8}Co_{0.1}Mn_{0.1}O_2$ (NMC811). For this battery, we used Li foil as the anode and $LiPF_6$/PC as the electrolyte. LiF was also detected in the CEI after being charged to 4.3 V (versus Li/Li^+), as confirmed by XPS (in Figure S9). For other transition metal oxide-based cathodes in $LiPF_6$ containing electrolytes, LiF was also detected in CEI.[25–28] Therefore, using Ti as the cathode electrode for LiF crystal investigation is reasonable. In future *in situ* liquid cell TEM experiments, adding Li-metal sources as well as additional reference electrodes in the electrochemical liquid cell is necessary for a direct comparison of the electrochemical reactions under TEM with those in real Li-ion batteries.

Nucleation, growth, moving, merging, and dissolution of LiF nanocrystals

For LiF nanosheet nucleation and growth in battery electrolytes, instead of one large nanosheet formed on the Ti electrode in a fixed position (shown in Figures 2A–2F and Video S1), small nanosheets with detachable or movable features were also captured on Ti electrode, as shown in Figures 3A–3F and in Video S2. Figures 3G–3L are the simulated 3D LiF crystals corresponding to Figures 3A–3F. Figures 3A and 3G show a bare Ti electrode with no LiF nanosheet deposited on it. As mentioned before, some dark spots on the Ti electrode are from residual photoresists during the E-cell fabrication process (see Figure S2A). Dark spots are also observed in Video S2 (see Figures S2B and S10). There are seven dark spots on the SiN_x area and the Ti electrode area (marked with black circles). From Figures S10A–S10F, these seven spots remain unchanged in the whole process (see the comparison between Figures S10A and S10F), which means they do not participate in the reaction. In comparison with Figure S10A, there are some newly emerging dark spots as shown in Figures S10B–S10E. We assign them to LiF nanocrystals, which is confirmed by the SAED pattern shown in Figure 2P. The LiF nanosheets mainly formed on Ti electrodes in the period of 0–11 s (Figures 3A–3E), during which time the Ti electrode was positively charged. The LiF deposition behavior is consistent with Figure 2 and Video S1. The difference with Figure 2 (Video S1) is that LiF
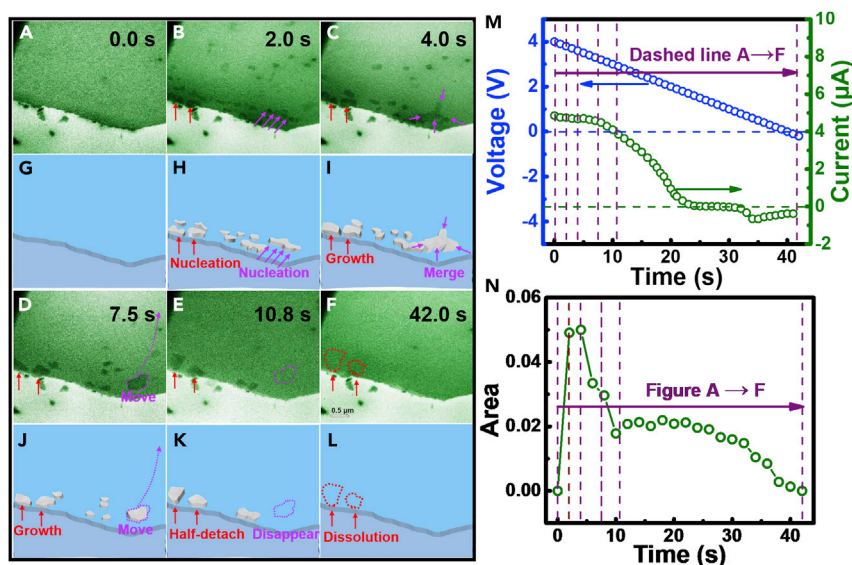
Figure 3. Deposition behaviors of LiF nanocrystals on Ti electrode

(A–F) Time series of TEM images illustrate the formation of LiF nanosheets on Ti electrodes and the flake movement on Ti electrodes.

(G–L) 3D images corresponding to (A)–(F) display the nucleation, growth, merging, and detachment of LiF nanosheets.

(M) Corresponding voltage loaded on the electrochemical liquid cell and measured current from the electrochemical workstation.

(N) Whole-area evolution of LiF nanosheets as a function of time during cyclic voltammetry in the voltage range of 4 to 0 V, with a scan rate of 100 mV/s.

nanosheets formed in Figure 3 (Video S2) can detach from the Ti electrode and move under an electric field, while the LiF nanosheet formed in Figure 2 (Video S1) did not move. That is why the total projected area of the generated LiF nanosheets in Video S2 dramatically decreases during the electrochemical process in the liquid cell, as also shown in Figure 3N. Figures 3B and 3H elucidate the nucleation of LiF nanosheets on positively charged Ti electrodes at 3.8 V (versus PSE Ti). Then, nanosheets grow and merge at 3.6 V (versus PSE Ti) in Figures 3C and 3I, and nanosheets move at 3.25 V (vs PSE Ti) in Figures 3D and 3J. Then, the half-detachment and movement of LiF nanosheets caused disappearance at 2.92 V (versus PSE Ti) in Figures 3E and 3K. Finally, with the applied voltage decreasing from 4 to 0 V, the measured current changed from positive to negative (starting from 28.2 s), and the deposited nanosheets gradually dissolved, as shown in Figures 3F and 3L (also see Figure S11 and Video S2). Based on the observation of Figures 3A–3L and Video S2, for the first time, we directly observe the self-healing behavior of LiF nanocrystals, which is consistent with the previous literature.[57,58] Combining Figures 2A–2L (Video S1) with Figures 3A–3L (Video S2), we can conclude that LiF nanosheets can cover the surface of the cathode electrode to prevent the side reaction between electrode and electrolyte. If the film is broken during the charge-discharge process, this self-healing behavior of the LiF nanocrystal could greatly improve the cycle performance of the battery.

DFT calculations to elucidate the formation mechanism of LiF crystals

Since the structure of the 2D nanosheets was confirmed as crystalline LiF by SAED (Figure 2P), albeit with many defects such as grain boundaries and not perfectly stoichiometric, its formation mechanism attracted our attention. To further elucidate the LiF deposition mechanism on positively charged Ti electrodes, joint DFT (JDFT)
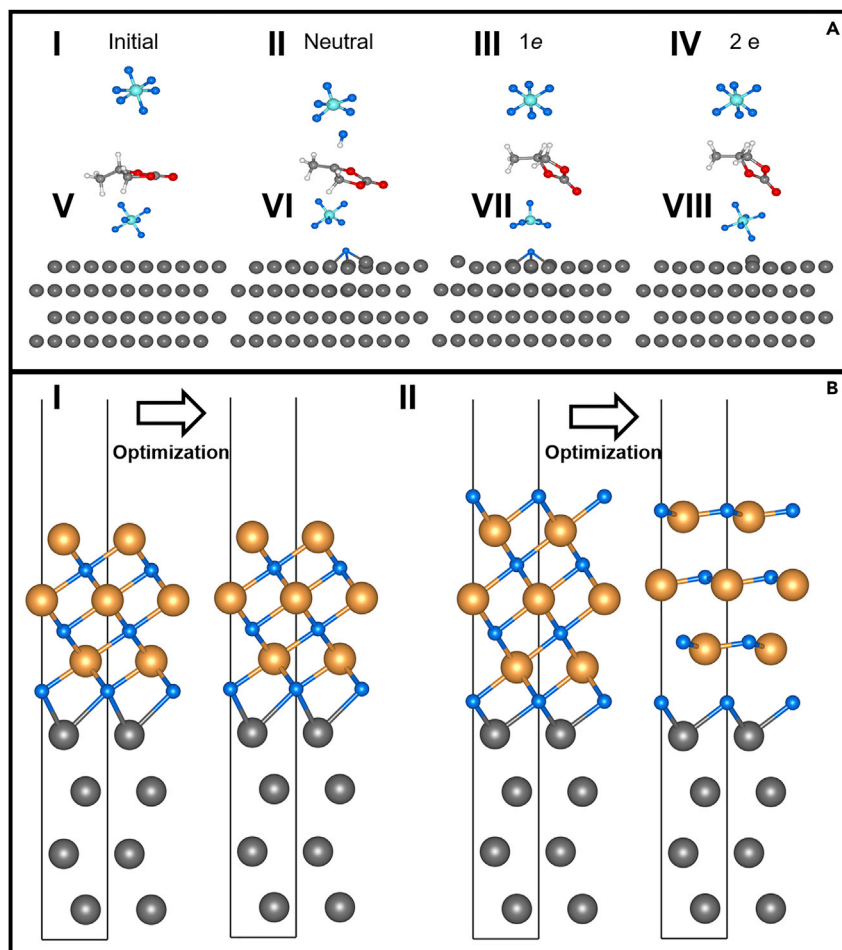
Figure 4. Theoretical calculation of PF_6^- decomposition near PC solvent or on Ti electrodes

(A) Decomposition of PF_6^- near (I)–(IV) PC solvent and (V)–(VIII) Ti electrode. Initial configurations of (I) PF_6 + PC and (V) PF_6 + Ti_n are shown in the first column. Optimized configurations of (II) PF_6^- + PC^+, (III) PF_6^- + PC, (IV) PF_6^- + PC^-, (VI) PF_6^- + Ti_n^+, (VII) PF_6^- + Ti_n, and (VIII) PF_6^- + Ti_n^- are shown in the second to fourth columns. All of the configurations are surrounded by implicit solvent. The number of additional electrons in JDFT are listed above the configurations. Atoms C, O, H, Ti, P, and F are light gray, red, white, heavy gray, cyan, and blue, respectively.

(B) Side view of structural optimization of (I) Li terminated and (II) F terminated LiF/Ti interface. Atoms Ti, Li, and F are gray, orange, and blue, respectively. The boundaries of the surface slabs are marked by black lines.

simulation was used to investigate the charged electrolyte/electrode interface at atomistic and electronic scales. The simulations in this section attempt to answer the following questions: (1) how did fluoride ions dissociate from $LiPF_6$ and (2) how did LiF grow on the Ti electrode and then detach?

Generally speaking, on the negative electrode, the LiF in SEI was a decomposition product of fluorinated ions, solvents, and additives on the anode surface. Here, the decompositions of PF_6^- in two different environments, either near the PC solvent or on the Ti electrode, were investigated. As shown in Figure 4, in the first case, PF_6^- and PC^+ spontaneously decompose into PF_5, $C_4H_5O_3$, and hydrogen fluoride (HF) (Figure 4A, II), while PF_6^- is stable near neutral and negatively charged PC (Figure 4A, III and IV). The structure-optimization trajectory can be found in Videos S3 and S4. The decomposition of PF_6^- was simulated by the JDFT method
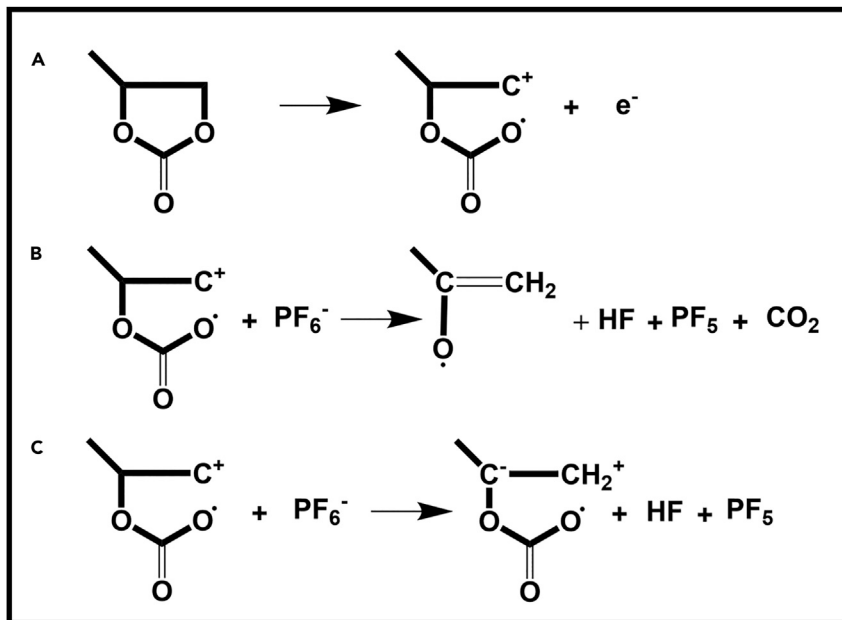
Matter
Article

 CellPress

Figure 5. Oxidation of PC and its product promotes the decomposition of PF_6^-
(A) Production of PC^+ via oxidation of PC.
(B and C) Two paths that PC^+ promotes the decomposition of PF_6^-.

(Figure S12A), which is a combination of explicit solute system (DFT simulation) and implicit solvent system (continuum model). The decomposition of PF_6^- and the charge transfer with the neighboring molecule/electrode was simulated by DFT simulation in Figure S12B, while the solvation interaction (i.e., the solvation shell of PC molecules), was simulated by the implicit solvent model in Figure S12C. When the decomposition of PF_6^- was investigated at positive and negative charged states in Figure 4A, the existence of a counter charge (Figure S12D) was also incorporated into the implicit solvent model by solving a Poisson-Boltzmann-type equation. Note that PC can be oxidized to PC^+ on the positively charged Ti electrode. In agreement with the simulation results, the current increases along with the voltage for two electrolytes (LiPF$_6$ in PC, PC only) in the CV curves, which occurs at a voltage higher than 3.6 V vs Li/Li$^+$ (Figures S7A and S7D). Here, the increment of the current is much higher in 1 M LiPF$_6$/PC than that in the PC solvent only, which is due to the solute conductivity effect. Specifically, two oxidation peaks were observed in Figure S7A. The peak at $\sim$4.7 V corresponds to the oxidation of PC and the decomposition of LiPF$_6$,[59] and the sharp increase of current at >5 V originated from the decomposition of PC. The oxidation product of PC is a positively charged radical[37] shown in Figure 5A, which is in agreement with the conclusion from Figure 4A, II. The radical can react with PF_6^- and form HF, as shown in Figures 5B and 5C. Then, the combination between HF and Li$^+$ can be one path to generate LiF, due to the limited solubility of LiF in PC.[60]

Besides the reaction with solvent PC, the decomposition of PF_6^- on Ti electrode surface was investigated in Figure 4A, V–VIII. It was found that PF_6^- was only stable near a negatively charged Ti electrode in Figure 4A, VIII. Spontaneous fluorine transfer from PF_6^- to Ti can be observed on positively charged and electrically neutral electrode surfaces in Figure 4A, VI and VII, respectively. The top view of the fluorinated Ti (0001) surface is shown in Figure S13. Therefore, F$^-$ of LiF on positively charged Ti electrodes is generated by the decomposition of PF_6^-. On negatively charged

CellPress

Matter
Article

Ti electrodes, PF_6^- shows enough stability and is repelled by electrostatic interaction from Ti electrodes; thus, the formation of LiF by this route is difficult. The different stability of PF_6^- at positive and negative potential can be used to understand the different deposition components observed on the cathode (LiF deposition) and anode (Li deposition) in experiments.

Importantly, two types of PF_6^- decomposition in Figures 4A, II and VI dominate the LiF formation on the positively charged electrode. The decomposition energy (E_D) of PF_6^- in the two reaction routes was calculated as follows:

or

$$E_D = E_{tot} - E_{PF_6^-} - E_{PC^+} \qquad \text{(Equation 1)}$$

$$E_D = E_{tot} - E_{PF_6^-} - E_{Ti_n^+} \qquad \text{(Equation 2)}$$

where E_D is the decomposition energy; E_{tot} is the system energy after PF_6^- decomposition in Figures 4A, II and VI; and $E_{PF_6^-}$, E_{PC^+}, and $E_{Ti_n^+}$ are the energies of charged reactants. Both the E_D of PF_6^- next to PC^+ in Figure 4A, II (-4.44 eV) and PF_6^- next to Ti_n^+ in Figure 4A, VI (-3.36 eV) are quite low, which indicates the spontaneous decomposition of PF_6^- near or on the positive Ti electrode. The decomposition of PF_6^- next to PC^+ (-4.44 eV) is favored slightly more than that on the positive Ti electrode (-3.36 eV). Thus, an initially charge-neutral PC solvent molecule can serve as a pathway or intermediary agent to transfer hole/oxidation to PF_6^-.

In Figures 3D and 3E, it was observed that the LiF film can desorb and move away from the Ti electrode. To understand the cause, the Ti/LiF interface was simulated (Figure 4B, I and II). Two models were constructed: three layers of F and three layers of Li on the Ti surface (Figure 4B, I), and four layers of F and three layers of Li on the Ti surface (Figure 4B, II). The simulation results indicate that if the layer number of F is equal to that of Li, there is nearly no difference between initial and optimized configurations. However, if there is one more F layer involved, then three layers of 2D like LiF layers are generated. At the same time, chemical bonding between 2D LiF and F-terminated Ti surface break down. The strong electronegativity of F is believed to be the origin of this interface reconstruction. The breaking of chemical bonds between the fluorinated Ti surface and 2D LiF can be the reason for the detachment of the LiF film.

Based on the *in situ* experimental results and theoretical calculations, we summarized the nucleation, growth, merging, detachment, movement, and dissolution behaviors of LiF nanocrystals on the Ti electrode and the corresponding $LiPF_6$/PC electrolyte decomposition mechanism in Figure 6. As shown in Figure 6A, with two Ti electrodes immersed in $LiPF_6$/PC electrolyte and then a voltage program (e.g., CV, linear sweep voltammetry) applied to the Ti electrodes, on positively charged Ti electrodes, we can see several LiF nanocrystals nucleated (Figure 6A, I), and subsequently, some grown LiF nanocrystals merged together (Figure 6A, II). During this positively charged state of Ti electrodes, the detachment of the LiF crystal was also observed (Figure 6A, III). Finally, when we reversed the charge state of the Ti electrode from positive to negative, the dissolution behavior of the merged LiF crystal was observed, with the detached LiF crystal moving away and disappearing (Figure 6A, IV). For the electrolyte decomposition mechanism, as shown in Figure 6B, there are two types of electrolyte decomposition and LiF formation paths on positively charged Ti electrodes. One is negative F^- ions transferring directly from the PF_6^- to the Ti electrode and the decomposed F^- ions combine with Li^+ ions and generate LiF (Figure 6B, I); the other is by an intermediary agent of PC: PC is oxidized first, and PC^+ promotes the decomposition of PF_6^-, which leads to the formation of HF, and the generated HF provides the F^- ions for the formation of LiF nanocrystal (Figure 6B, II).
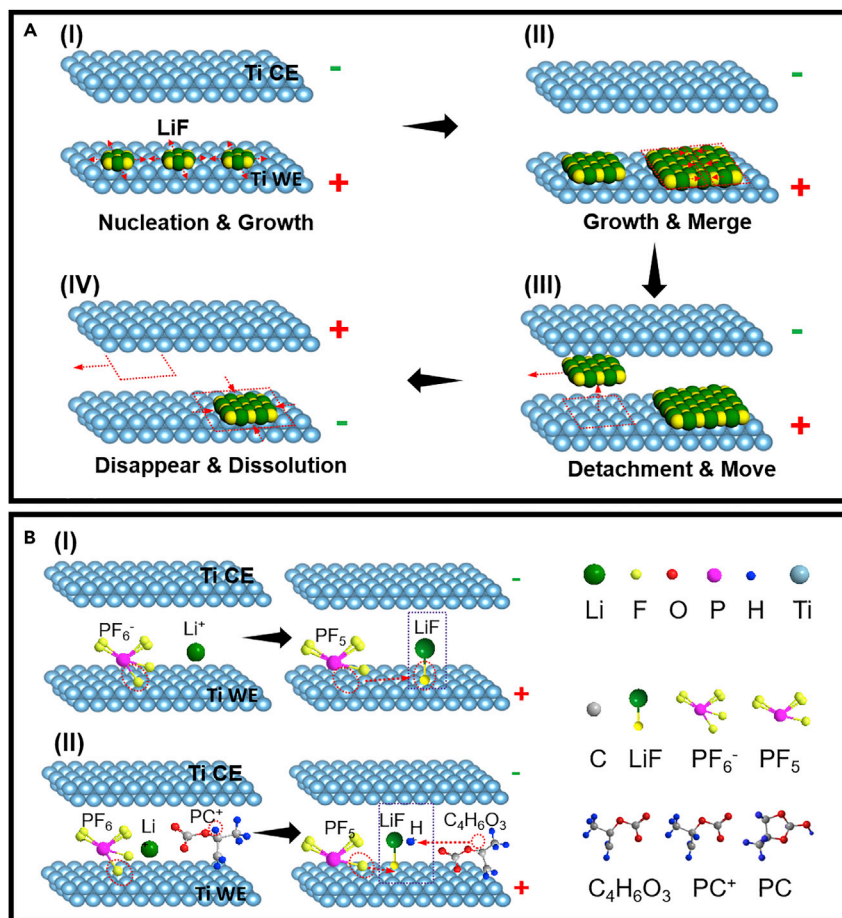
CellPress

Figure 6. Formation paths of LiF crystal on positively charged Ti electrodes and its behaviors on the electrode

(A) Schematic of nucleation, growth, merging, detachment, movement, and dissolution behaviors of LiF nanosheets on Ti electrodes in the electrochemical liquid cell during the cyclic voltammetry test.

(B) Two formation paths of LiF nanosheets on positively charged Ti electrodes due to the $LiPF_6$/PC electrolyte decomposition in the electrochemical liquid cell.

Lastly, we need to point out that electron-beam effects are unavoidable in *in situ* TEM experiments. Nonetheless, beam effects can be minimized at the reduced electron dose during imaging. To confirm that LiF deposition is not caused by e-beam irradiation, control experiments were conducted with the same low electron beam dose (<1 $e\text{Å}^{-2}$ s^{-1}), but without the programmed CV applied to the electrochemical liquid cell. The captured video data indicate that no deposition or reactions happened on the Ti electrode under such a low beam intensity, even for an extended period. In addition, we conducted extra experiments by blocking the beam in a periodic manner, and no obvious difference occurred in the LiF deposition behavior. Another point to mention is that to achieve high spatial resolution of the deposited LiF nanocrystals in an electrochemical liquid cell, the liquid layer needs to be evenly distributed with a thickness equal to 150 nm. This differs from real battery configuration since real battery electrodes are separated by a porous separator (e.g., polypropylene film). In this case, the liquid layer is porous by filling the pores or voids of the separator; hence, the morphology of the deposited LiF crystals in the real cathode electrode may be

 CellPress

Matter
Article

different from the morphology observed in the liquid cell and may need more advanced techniques to image in the future.

Conclusions

In summary, we have conducted a systematic study on the formation of LiF nanosheets on positively charged Ti electrodes through a combination of experimental data and theoretical calculations. *In situ* TEM observations illustrate the nucleation, growth, merging, detachment, and movement of LiF nanocrystals on positively charged Ti electrodes and the dissolution of LiF nanocrystals when the electrode becomes less positively charged. Theoretical calculations demonstrated that an intermediary PC^+ can promote the decomposition of PF_6^-. Fluorine can transfer from PF_6^- to positively charged or electrically neutral Ti electrodes spontaneously. Both paths can provide fluorine to form LiF naonsheets, and if the formed LiF is terminated by F on Ti electrodes, inter-surface reconstruction is induced by the electronegativity of F, which may result in the detachment and movement of LiF flakes during electrochemical reactions. Our *in situ* study of LiF formation on the CEI proves that the LiF crystal has remarkable morphing mobility and self-healing ability, which provides valuable insights on improving the cathode surface chemistry for improved battery performance and cycle life.

EXPERIMENTAL PROCEDURES

Resource availability

Lead contact

Further information and requests for resources and reagents should be directed to and will be fulfilled by the lead contact, Zhiyuan Zeng (zhiyzeng@cityu.edu.hk).

Materials availability

This study did not generate new unique reagents.

Data and code availability

The data that support the plots within this article, and other findings of this study, are available from the corresponding authors upon reasonable request.

Materials and methods

Fabrication of electrochemical liquid cell

The fabrication procedure of the electrochemical liquid cell is similar to our previous work.[48,50] The liquid cells, including bottom and top chips, were fabricated using ultra-thin silicon wafers (200 μm, 4 inches, p-doped) purchased from Virginia Semiconductor (Fredericksburg, VA). A 25-nm-thick low-stress silicon nitride film was evaporated on the silicon wafer as a membrane of the viewing window. The viewing windows and two reservoirs were created by photolithographic patterning and etching with KOH solution (with a water:KOH ratio of 2:1). The dimensions of the windows are 25 × 6 μm. Two 90-nm-thick Ti electrodes were deposited on the bottom chips with a face-to-face distance of 20 μm. The bottom and top chips were sealed using a 150-nm-thick sputtered indium spacer. A total of 1 M $LiPF_6$ dissolved in PC, was loaded into the reservoirs with a syringe in a glove box. Liquid electrolyte flowed into the viewing window by capillary force. We sealed the cell, including the reservoirs, using Cu foil and epoxy. Since the window gap is no larger than 150 nm, no contamination from epoxy was observed during the electrochemical experiments. The dimensions of a biasing cell are ∼3 mm × 3 mm square and ∼400 μm thick. The nano-battery was put into a home-made TEM holder for TEM characterization under bias. Both of the WE and CE were extended to two Ti pads in two reservoirs.

Matter
Article

 CellPress

Al wires were bonded onto each Ti pad. The bonded Al wires were connected to the two Cu pads on the customized TEM holder tip. The TEM holder fits a JEOL 2100 TEM.

Two patterned Ti electrodes were used as a WE, CE, and reference electrode, respectively. The electrolyte was 1 M $LiPF_6$ dissolved in PC. The two electrode configurations were assembled in a clean room.

Characterizations

Real-time videos shown in Figures 2 and 3 of the dynamic electrochemical reactions were recorded using a JEOL 2100 TEM microscope operating at 200 kV, which was equipped with a Gatan Orius camera-facilitated frame rate of 30 fps. TEM images and SAED pattern were acquired using a JEOL 2100 TEM microscope. The electrochemical process was controlled by an electrochemical workstation (CH Instruments, model 660D series). It was used to perform *in situ* CV measurements with a voltage range of 4 to −4 V and a scan rate of 100 mV/s. The *ex situ* CV curves presented in Figure S7 were measured by an electrochemical workstation (Ivium-N-stat) with a three-electrode configuration. The WE was cycled between 1.0 and 5.6 V Li/Li$^+$, and the scan rate was 0.1 mV/s. It was used to confirm the variation of potential of Ti CEs during measurement. The XPS spectra were recorded by Thermo Scientific K-Alpha with monochromatic 150-W Al Kα radiation. The binding energies were referenced to the C 1 s line at 284.8 eV from adventitious carbon. For XPS characterization, a battery charged to 4.3 V was disassembled in an Ar-filled glove box and the NMC811 electrode was washed with DMC to remove $LiPF_6$.

DFT calculations

All of the spin-polarized DFT calculations were performed by the Vienna Ab-initio Simulation Package (VASP)[61,62] using projector-augmented wave (PAW) pseudo-potentials[63] and the Perdew-Burke-Ernzerhof (PBE) functional.[64] The cutoff energy for the plane-wave basis was 600 eV. Electrons in the states of (3d, 4s) of Ti, (1s) of H, (1s, 2s, 2p) of Li, and (2s, 2p) of C, O, F, and P were considered valence electrons. 11 × 11 × 1-, 6 × 6 × 1-, and 3 × 3 × 1-k point grids were used for 1 × 1, 2 × 2, and 4 × 4 surface slabs. There are four layers in the Ti surface slab model and the bottom layer was fixed. The thickness of the vacuum/solution region in the z direction is ∼30 Å. In the simulation of ion and solvent decomposition, the space without atoms was filled with implicit solvent by the JDFT method, which was coded in VASPsol.[65,66] The dielectric constant ε_r of solvent PC was set to 64.0 and the ion concentration was 1 M. Other parameters of the solvation model were not changed. In charged systems, the number of electrons in JDFT was changed, and this part of the charge was screened by the implicit solvation model by solving the linearized Poisson-Boltzmann equation in VASPsol. The convergence for electronic energy and structural optimization was set at 1×10^{-6} and 0.02 eV/Å.

SUPPLEMENTAL INFORMATION

Supplemental information can be found online at https://doi.org/10.1016/j.matt.2022.01.015.

CellPress

Matter
Article

AUTHOR CONTRIBUTIONS

Z.Z. conceived and directed the project. Z.Z. performed the *in situ* TEM experiments. Q.Z. performed the electrochemical experiments and the XPS characterizations. J.M. and Z.L. performed the computational simulations. Q.Z., J.M., J.L., and Z.Z. co-wrote the manuscript. J.L. envisioned the manuscript, with input from all of the authors.

DECLARATION OF INTERESTS

The authors declare no competing interests.

REFERENCES

1. Feng, X.N., Ouyang, M.G., Liu, X., Lu, L.G., Xia, Y., and He, X.M. (2018). Thermal runaway mechanism of lithium ion battery for electric vehicles: a review. Energy Storage Mater. *10*, 246–267.

2. Barré, A., Deguilhem, B., Grolleau, S., Gérard, M., Suard, F., and Riu, F. (2013). A review on lithium ion batteries ageing mechanisms and estimation for automative applications. J. Power Sources *241*, 680–689.

3. Buqa, H., Würsig, A., Vetter, J., Spahr, M.E., Krumeich, F., and Novák, P. (2006). SEI film formation on highly crystalline graphitic materials in lithium-ion batteries. J. Power Sources *153*, 385–390.

4. Yang, R.J., Mei, L., Zhang, Q.Y., Fan, Y.Y., Shin, H.S., Voiry, D., and Zeng, Z.Y. (2021). High-yield production of mono- or few-layer transition metal dichalcogenide nanosheets by electrochemical lithium ion intercalation-based exfoliation method. Nat. Protoc. https://doi.org/10.1038/s41596-021-00643-w.

5. Zeng, Z.Y., Liang, W.I., Chu, Y.H., and Zheng, H.M. (2014). In situ TEM study of the Li-Au reaction in an electrochemical liquid cell. Faraday Discuss. *176*, 95–107.

6. Zeng, Z.Y., Barai, P., Lee, S.Y., Yang, J., Zhang, X.W., Zheng, W.J., Liu, Y.S., Bustillo, K.C., Ercius, P., Guo, J.H., et al. (2020). Electrode roughness dependent electrodeposition of sodium at the nanoscale. Nano Energy *72*, 104721.

7. Zeng, Z.Y., Zheng, W.J., and Zheng, H.M. (2017). Visualization of colloidal nanocrystal formation and electrode-electrolyte interfaces in liquids using TEM. Acc. Chem. Res. *50*, 1808–1817.

8. Ma, L., Glazier, S.L., Petibon, R., Xia, J., Peters, J.M., Liu, Q., Allen, J., Doig, R.N.C., and Dahn, J.R. (2016). A guide to ethylene carbonate-free electrolyte making for Li-ion cells. J. Electrochem. Soc. *164*, A5008–A5018.

9. He, Y., Jiang, L., Chen, T.W., Xu, Y.B., Jia, H.P., Yi, R., Zhang, S.L., Wang, C.M., Xue, D.C., Song, M., et al. (2021). Progressive growth of the solid-electrolyte interphase towards the Si anode interior causes capacity fading. Nat. Nanotechnol. *16*, 1113–1120.

10. Takenaka, N., Suzuki, Y., Sakai, H., and Nagaoka, M. (2014). On electrolyte-dependent formation of solid electrolyte interphase film in lithium-ion batteries: strong sensitivity to small structural difference of electrolyte molecules. J. Phys. Chem. C *118*, 10874–10882.

11. Peled, E., Golodnitsky, D., and Ardel, G. (1997). Advanced model for solid electrolyte interphase electrodes in liquid and polymer electrolytes. J. Electrochem. Soc. *144*, L208–L210.

12. Lu, P., Li, C., Schneider, E.W., and Harris, S.J. (2014). Chemistry, impedance, and morphology evolution in solid electrolyte interphase films during formation in lithium ion batteries. J. Phys. Chem. C *118*, 896–903.

13. Peled, E., and Menkin, S. (2017). Review-SEI: past, present and future. J. Electrochem. Soc. *164*, A1703–A1719.

14. Wang, L.N., Menakath, A., Han, F.D., Wang, Y., Zavalij, P.Y., Gaskell, K.J., Borodin, O., Iuga, D., Brown, S.P., Wang, C.S., et al. (2019). Identifying the components of the solid-electrolyte interphase in Li-ion batteries. Nat. Chem. *11*, 789–796.

15. Shadike, Z., Lee, H., Borodin, O., Cao, X., Lin, R.Q., Bak, S.M., Ghose, S., Xu, K., Xiao, J., Yang, X.Q., and Hu, E.Y. (2021). Identification of LiH and nanocrystalline LiF in the solid-electrolyte interphase of lithium metal anodes. Nat. Nanotechnol. *16*, 549–554.

16. Zhou, Y.F., Cao, R.G., Wang, X.L., Su, M., Yu, X.F., Zhang, Y.Y., Wang, J.G., Ren, X.D., Xu, W., Xu, K., Baer, D.R., Du, Y.G., Xu, Z.J., Borodin, O., Wang, C.M., and Zhu, Z.H. (2020). Real-time mass spectrometric characterization of the solid-electrolyte interphase of a lithium-ion battery. Nat. Nanotechnol. *15*, 224–230.

17. Han, X.P., and Sun, J. (2020). Design of a LiF-rich solid electrolyte interface layer through salt-additive chemistry for boosting fast-charging phosphorus-based lithium ion battery performance. Chem. Commun. (Camb). *56*, 6047–6049.

18. Li, T., Zhang, X.Q., Shi, P., and Zhang, Q. (2019). Fluorinated solid-electrolyte interphase in high-voltage lithium metal batteries. Joule *3*, 2647–2661.

19. Chen, J., Fan, X.F., Li, Q., Yang, H.B., Khoshi, M.R., Xu, Y.B., Hwang, S., Chen, L., Ji, X., Yang, C.Y., et al. (2020). Electrolyte design for LiF-rich solid–electrolyte interfaces to enable high-performance microsized alloy anodes for batteries. Nat. Energy *5*, 386–397.

20. Zhang, L., Zhang, K.H., Shi, Z.H., and Zhang, S.J. (2017). LiF as an artificial SEI layer to enhance the high temperature cycle performance of LTO. Langmuir *33*, 11164–11169.

21. Wang, M.Q., Peng, Z., Luo, W.W., Ren, F.H., Li, Z.D., Zhang, Q., He, H.Y., Ouyang, C.Y., and Wang, D.Y. (2019). Tailoring lithium deposition via an SEI-functionalized membrane derived from LiF decorated layered carbon structure. Adv. Energy Mater. *9*, 1802912.

22. Xue, W.J., Huang, M.H., Li, Y.T., Zhu, Y.G., Gao, R., Xiao, X.H., Zhang, W.X., Li, S.P., Xu, G.Y., Yu, Y., et al. (2021). Ultra-high-voltage Ni-rich layered cathodes in practical Li metal batteries enabled by a sulfonamide-based electrolyte. Nat. Energy *6*, 495–505.

Matter
Article

CellPress

23. Ren, X.D., Zhang, X.H., Shadike, Z., Zou, L.F., Jia, H., Cao, X., Engelhard, M.H., Matthews, B.E., Wang, C.M., Arey, B.W., et al. (2020). Designing advanced in situ electrode/electrolyte interphases for wide temperature operation of 4.5 V Li||LiCoO₂ batteries. Adv. Mater. *32*, 2004898.

24. Aurbach, D., Gamolsky, K., Markovsky, B., Salitra, G., Gofer, Y., Heider, U., Oesten, R., and Schmidt, M. (2000). The study of surface phenomena related to electrochemical lithium intercalation into LiₓMOᵧ host materials (M = Ni, Mn). J. Electrochem. Soc. *147*, 1322–1331.

25. Zhang, J.N., Li, Q.H., Wang, Y., Zheng, J.Y., Yu, X.Q., and Li, H. (2018). Dynamic evolution of cathode electrolyte interphase (CEI) on high voltage LiCoO₂ cathode and its interaction with Li anode. Energy Storage Mater. *14*, 1–7.

26. Yoon, T., Soon, J.Y., Lee, T.J., Ryu, J.H., and Oh, S.M. (2021). Dissolution of cathode–electrolyte interphase deposited on LiNi₀.₅Mn₁.₅O₄ for lithium-ion batteries. J. Power Sources *503*, 230051.

27. Lebens-Higgins, Z.W., Sallis, S., Faenza, N.V., Badway, F., Pereira, N., Halat, D.M., Wahila, M., Schlueter, C., Lee, T.L., Yang, W.L., et al. (2018). Evolution of the electrode–electrolyte interface of LiNi₀.₈Co₀.₁₅Al₀.₀₅O₂ electrodes due to electrochemical and thermal stress. Chem. Mater. *30*, 958–969.

28. Zhao, W.G., Zheng, J.M., Zou, L.F., Jia, H.P., Liu, B., Wang, H., Engelhard, M.H., Wang, C.M., Xu, W., Yang, Y., and Zhang, J.G. (2018). High voltage operation of Ni-rich NMC cathodes enabled by stable electrode/electrolyte interphases. Adv. Energy Mater. *8*, 1800297.

29. Xiong, X.H., Zhixing Wang, Z.X., Yin, X., Guo, H.J., and Li, X.H. (2013). A modified LiF coating process to enhance the electrochemical performance characteristics of LiNi₀.₈Co₀.₁Mn₀.₁O₂ cathode materials. Mater. Lett. *110*, 4–9.

30. Shi, S.J., Tu, J.P., Tang, Y.Y., Zhang, Y.Q., Liu, X.Y., Wang, X.L., and Gu, C.D. (2013). Enhanced electrochemical performance of LiF-modified LiNi₁/₃Co₁/₃Mn₁/₃O₂ cathode materials for Li-ion batteries. J. Power Sources *225*, 338–346.

31. Andersson, A.M., Herstedt, M., Bishop, A.G., and Edstrom, K. (2002). The influence of lithium salt on the interfacial reactions controlling the thermal stability of graphite anodes. Electrochim Acta *47*, 1885–1898.

32. Parimalam, B.S., and Lucht, B.L. (2018). Reduction reactions of electrolyte salts for lithium ion batteries: LiPF₆, LiBF₄, LiDFOB, LiBOB, and LiTFSI. J. Electrochem. Soc. *165*, A251–A255.

33. Alvarado, J., Schroeder, M.A., Zhang, M.H., Borodin, O., Gobrogge, E., Olguin, M., Ding, M.S., Gobet, M., Greenbaum, S., Meng, Y.S., and Xu, K. (2018). A carbonate-free, sulfone-based electrolyte for high-voltage Li-ion batteries. Mater. Today *21*, 341–353.

34. Leung, K. (2015). Predicting the voltage dependence of interfacial electrochemical processes at lithium-intercalated graphite edge planes. Phys. Chem. Chem. Phys. *17*, 1637–1643.

35. Nova, P., Christensen, P.A., Iwasita, T., and Vielstich, W. (1989). Anodic oxidation of propylene carbonate on platinum, glassy carbon and polypyrrole an "in-situ" FTIR study. J. Electroanal. Chem. *263*, 37–48.

36. Borodin, O. (2019). Challenges with prediction of battery electrolyte electrochemical stability window and guiding the electrode – electrolyte stabilization. Curr. Opin. Electrochem. *13*, 86–93.

37. Kanamura, K., Toriyama, S., Shiraishi, S., and Takehara, Z. (1995). Studies on electrochemical oxidation of nonaqueous electrolytes using in situ FTIR spectroscopy I . The effect of type of electrode on on-set potential for electrochemical oxidation of propylene carbonate containing 1.0 mol dm⁻³ LiClO₄. J. Electrochem. Soc. *142*, 1383–1389.

38. Kanamura, K., Toriyama, S., Shiraishi, S., Ohashi, M., and Takehara, Z. (1996). Studies on electrochemical oxidation of non-aqueous electrolyte on the LiCoO₂ thin film electrode. J. Electroanal. Chem. *419*, 77–84.

39. Yu, Y., Karayaylali, P., Katayama, Y., Giordano, L., Gauthier, M., Maglia, F., Jung, R., Lund, I., and Shao-Horn, Y. (2018). Coupled LiPF₆ decomposition and carbonate dehydrogenation enhanced by highly covalent metal oxides in high-energy Li-ion batteries. J. Phys. Chem. C *122*, 27368–27382.

40. Solchenbach, S., Metzger, M., Egawa, M., Beyer, H., and Gasteiger, H.A. (2018). Quantification of PF₅ and POF₃ from side reactions of LiPF₆ in Li-ion batteries. J. Electrochem. Soc. *165*, A3022–A3028.

41. Tasaki, K., Goldberg, A., Lian, J.-J., Walker, M., Timmons, A., and Harris, S.J. (2009). Solubility of lithium salts formed on the lithium-ion battery negative electrode surface in organic solvents. J. Electrochem. Soc. *156*, A1019–A1027.

42. Dedryvère, R., Martinez, H., Leroy, S., Lemordant, D., Bonhomme, F., Biensan, P., and Gonbeau, D. (2007). Surface film formation on electrodes in a LiCoO₂/graphite cell: a step by step XPS study. J. Power Sources *174*, 462–468.

43. Kanamura, K., Tamura, H., and Takehara, Z.-I. (1992). XPS analysis of a lithium surface immersed in propylene carbonate solution containing various salts. J. Electroanal. Chem. *333*, 127–142.

44. Lee, S.H., You, H.G., Han, K.S., Kim, J., Jung, I.H., and Song, J.H. (2014). A new approach to surface properties of solid electrolyte interphase on a graphite negative electrode. J. Power Sources *247*, 307–313.

45. Murakami, M., Yamashige, H., Arai, H., Uchimoto, Y., and Ogumi, Z. (2011). Direct evidence of LiF formation at electrode/electrolyte interface by ⁷Li and ¹⁹F double-resonance solid-state NMR spectroscopy. Electrochem. Solid-State Lett. *14*, A134–A137.

46. Gauthier, N., Courrèges, C., Demeaux, J., Tessier, C., and Martinez, H. (2020). Probing the in-depth distribution of organic/inorganic molecular species within the SEI of LTO/NMC and LTO/LMO batteries: a complementary ToF-SIMS and XPS study. Appl. Surf. Sci. *501*, 144266.

47. Huang, W., Wang, H.S., Boyle, D.T., Li, Y.Z., and Cui, Y. (2020). Resolving nanoscopic and mesoscopic heterogeneity of fluorinated species in battery solid-electrolyte interphases by cryogenic electron microscopy. ACS Energy Lett. *5*, 1128–1135.

48. Zeng, Z.Y., Zhang, X.W., Bustillo, K., Niu, K.Y., Gammer, C., Xu, J., and Zheng, H.M. (2015). In situ study of lithiation and delithiation of MoS₂ nanosheets using electrochemical liquid cell transmission electron microscopy. Nano Lett. *15*, 5214–5220.

49. Liu, T., Lin, L., Bi, X., Tian, L., Yang, K., Liu, J., Li, M., Chen, Z., Lu, J., Amine, K., et al. (2019). In situ quantification of interphasial chemistry in Li-ion battery. Nat. Nanotechnol. *14*, 50–56.

50. Zeng, Z.Y., Liang, W.I., Liao, H.G., Xin, H.L., Chu, Y.H., and Zheng, H.M. (2014). Visualization of electrode-electrolyte interfaces in LiPF₆/EC/DEC electrolyte for lithium ion batteries via in situ TEM. Nano Lett. *14*, 1745–1750.

51. Rong, G.L., Zhang, X.Y., Zhao, W., Qiu, Y.C., Liu, M.N., Ye, F.M., Xu, Y., Chen, J.F., Hou, Y., Li, W.F., et al. (2017). Liquid-phase electrochemical scanning electron microscopy for in situ investigation of lithium dendrite growth and dissolution. Adv. Mater. *29*, 1606187.

52. Zhang, J., Wang, R., Yang, X.C., Lu, W., Wu, X.D., Wang, X.P., Li, H., and Chen, L.W. (2012). Direct observation of inhomogeneous solid electrolyte interphase on MnO anode with atomic force microscopy and spectroscopy. Nano Lett. *12*, 2153–2157.

53. Wang, L.X., Deng, D., Lev, L.C., and Ng, S. (2014). In-situ investigation of solid-electrolyte interphase formation on the anode of Li-ion batteries with Atomic Force Microscopy. J. Power Sources *265*, 140–148.

54. Wang, M.Q., Huai, L.Y., Hu, G.H., Yang, S.S., Ren, F.H., Wang, S.W., Zhang, Z.G., Chen, Z.L., Peng, Z., Shen, C., and Wang, D.Y. (2018). Effect of LiFSI concentrations to form thickness- and modulus-controlled SEI layers on lithium metal anodes. J. Phys. Chem. C *122*, 9825–9834.

55. Heiskanen, S.K., Kim, J.K., and Lucht, B.L. (2019). Generation and evolution of the solid electrolyte interphase of lithium-ion batteries. Joule *3*, 2322–2333.

56. Xu, Y.B., Wu, H.P., Jia, H., Zhang, J.-G., Xu, W., and Wang, C.M. (2020). Current density regulated atomic to nanoscale process on Li deposition and solid electrolyte interphase revealed by cryogenic transmission electron microscopy. ACS Nano *14*, 8766–8775.

57. Jin, Y., Li, S., Kushima, A., Zheng, X.Q., Sun, Y.M., Xie, J., Sun, J., Xue, W.J., Zhou, G.M., Wu, J., et al. (2017). Self-healing SEI enables full-cell cycling of a silicon-majority anode with a coulombic efficiency exceeding 99.9%. Energy Environ. Sci. *10*, 580–592.

58. Li, S., Jiang, M.W., Xie, Y., Xu, H., Jia, J.Y., and Li, J. (2018). Developing high-performance lithium metal anode in liquid electrolytes: challenges and progress. Adv. Mater. *30*, 1706375.

59. Zhou, H.M., Fang, Z.Q., and Li, J. (2013). LiPF₆ and lithium difluoro(oxalato) -borate/ethylene carbonate + dimethyl carbonate +

CellPress

Matter
Article

ethyl(methyl)carbonate electrolyte for $Li_4Ti_5O_{12}$ anode. J. Power Sources *230*, 148–154.

60. Jones, J., Anouti, M., Magaly, C.-C., Willmann, P., and Lemordant, D. (2009). Thermodynamic of LiF dissolution in alkylcarbonates and some of their mixtures with water. Fluid Phase Equilibria *285*, 62–68.

61. Kresse, G., and Furthmüller, J. (1996). Efficiency of ab-initio total energy calculations for metals and semiconductors using a plane-wave basis set. J. Comput. Mater. Sci. *6*, 15–50.

62. Kresse, G. (1996). Efficient iterative schemes for ab initio total-energy calculations using a plane-wave basis set. Phys. Rev. B. *54*, 11169–11186.

63. Kresse, G., and Joubert, D. (1999). From ultrasoft pseudopotentials to the projector augmented-wave method. Phys. Rev. B. *59*, 1758–1775.

64. Perdew, J.P., Burke, K., and Ernzerhof, M. (1996). Generalized gradient approximation made simple. Phys. Rev. Lett. *77*, 3865–3868.

65. Mathew, K., Sundararaman, R., Letchworth-Weaver, K., Arias, T.A., and Hennig, R.G. (2014). Implicit solvation model for density-functional study of nanocrystal surfaces and reaction pathways. J. Chem. Phys. *140*, 084106.

66. Mathew, K., Kolluru, V.S.C., Mula, S., Steinmann, S.N., and Hennig, R.G. (2019). Implicit self-consistent electrolyte model in plane-wave density-functional theory. J. Chem. Phys. *151*, 234101.

Supplemental information

In situ TEM visualization of LiF nanosheet

formation on the cathode-electrolyte interphase

(CEI) in liquid-electrolyte lithium-ion batteries

Qingyong Zhang, Jiale Ma, Liang Mei, Jun Liu, Zhenyu Li, Ju Li, and Zhiyuan Zeng

In-Situ TEM Visualization of 2D LiF Nanosheets Formation on the Cathode-Electrolyte Interphase (CEI) in Liquid-Electrolyte Lithium-Ion Batteries

Qingyong Zhang[#,1], Jiale Ma[#,3], Liang Mei[1], Jun Liu[4], Zhenyu Li[3*], Ju Li[5*], Zhiyuan Zeng[1,2*]
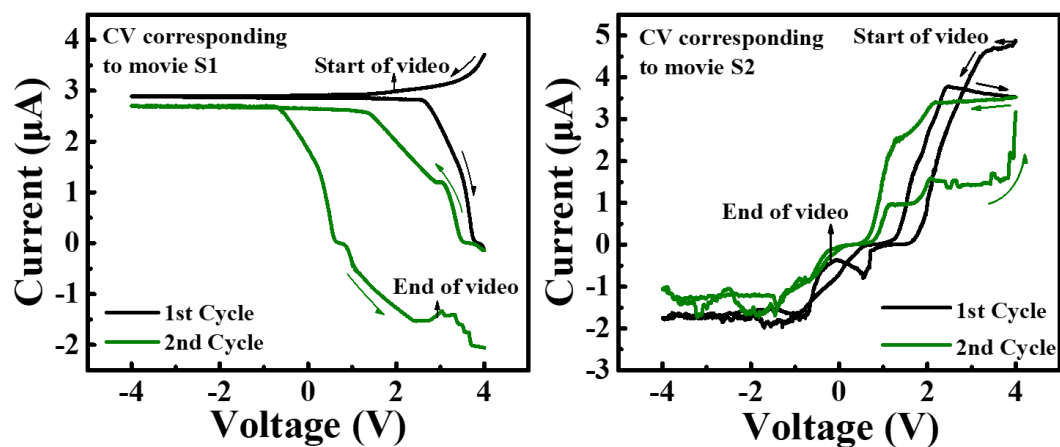
Figure S1. Cyclic voltammetry of Ti electrode in electrolyte of 1 M $LiPF_6$ in PC (Vs pseudo reference electrode Ti (PSE Ti)).
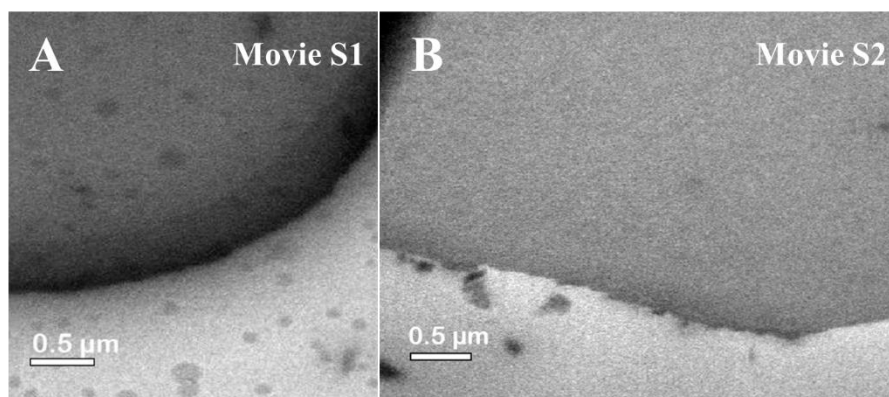
Figure S2. Morphologies of Ti electrodes at the beginning of in-situ Movies.
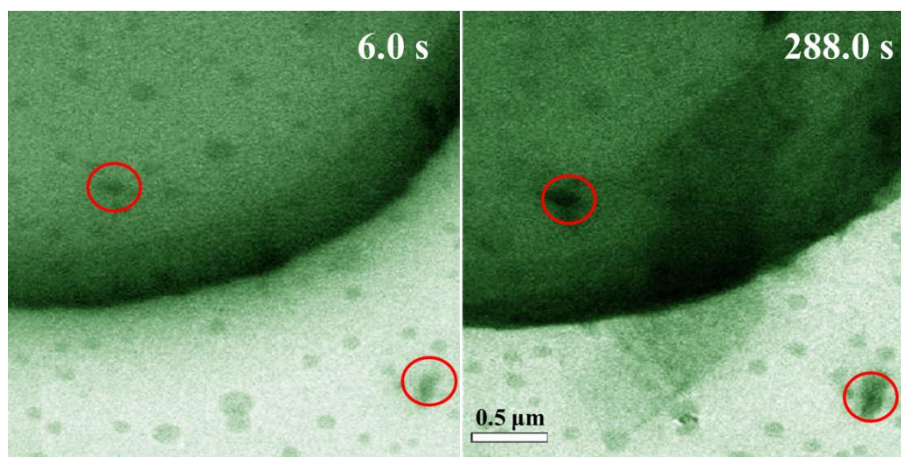
Figure S3. The observed changes of the dark points during in-situ TEM observation in Movie S1.
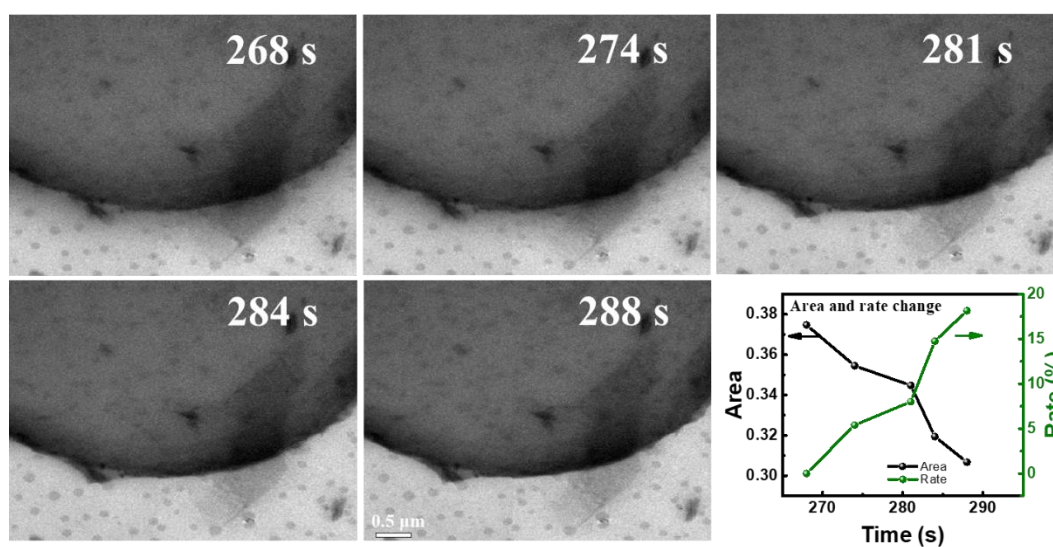
Figure S4. Area change of LiF nanosheet at time period 268 - 288 s under negative current in Movie S1. Area change rate (t) = [Area (268s) – Area (t)] / Area (268s).
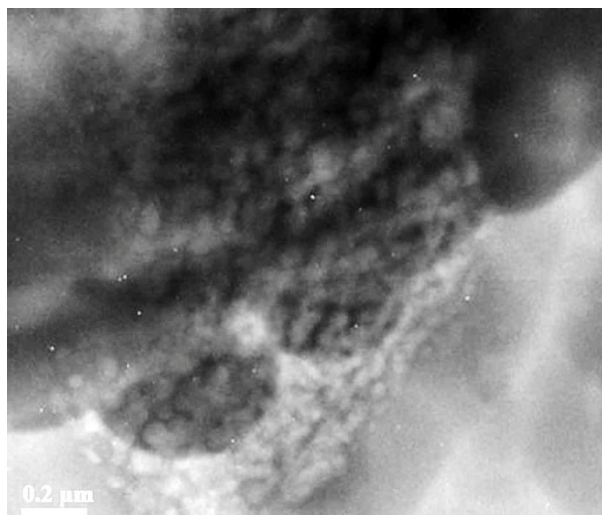
Figure S5. TEM image of the in-situ formed LiF nanosheets in the liquid cell.
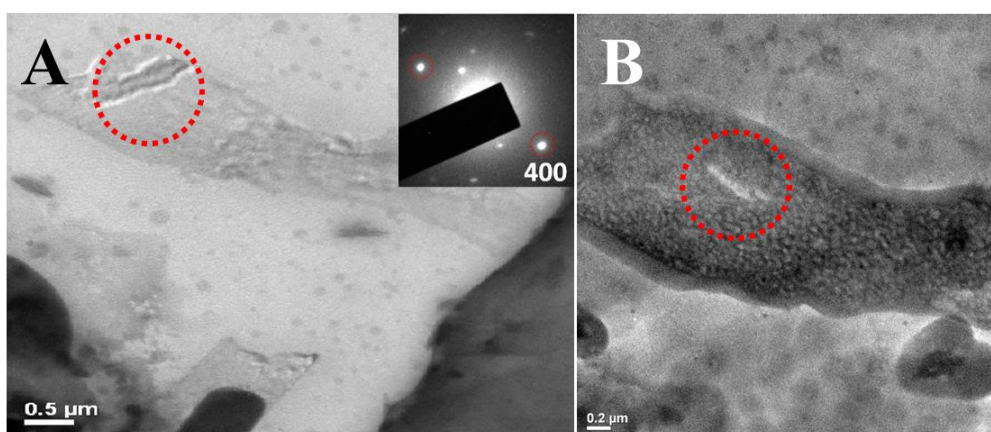
Figure S6. Morphology and the selected area electron diffraction (SAED) pattern of the ex-situ formed LiF nanosheets in the liquid cell.
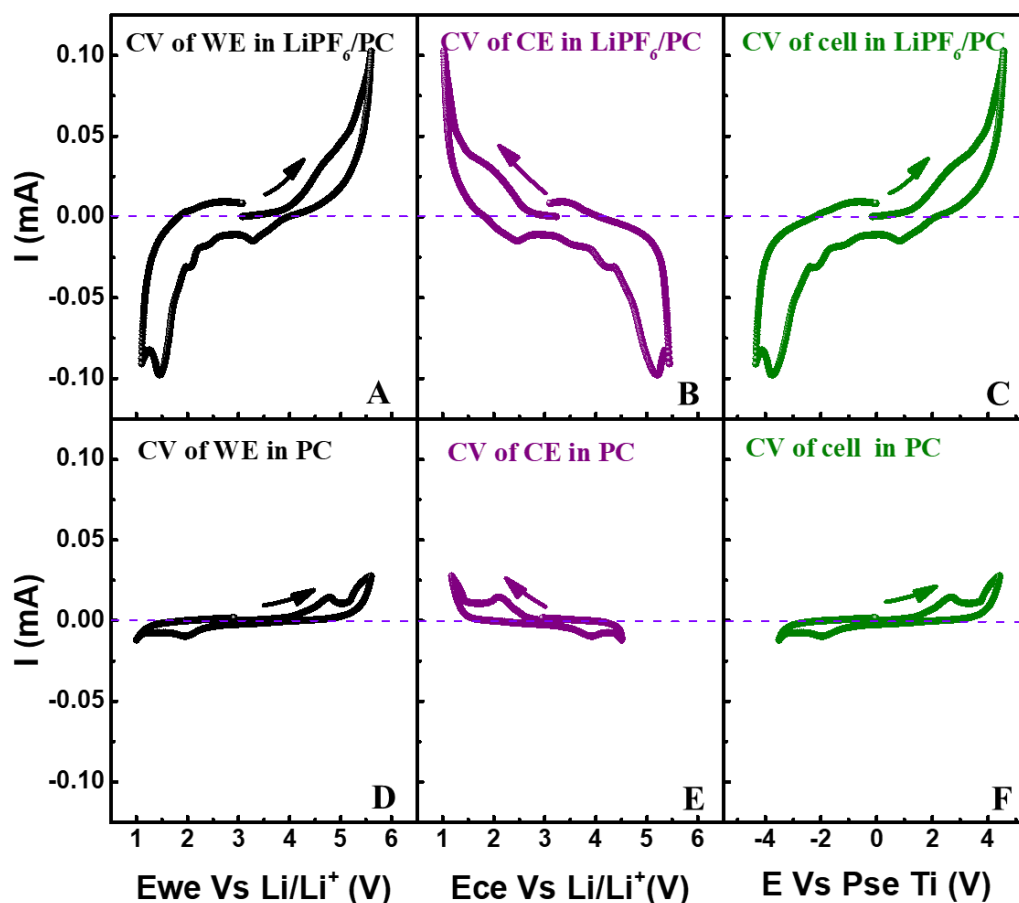
Figure S7. Cyclic voltammetry curve tested in three electrodes configuration at the scan rate of 0.1 mV/s with WE potential range 1.0 - 5.6 V Vs Li/Li$^+$.
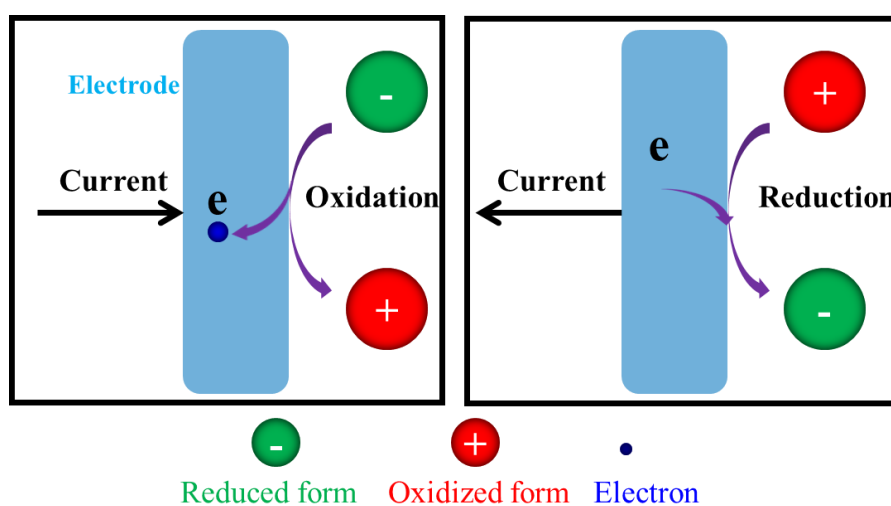
Figure S8. Schematic to show how to determine the state of electrode by current. Current flowing into electrode results in electrochemical oxidation, and reduced form is oxidized to oxidized form. Current flowing out of electrode results in electrochemical reduction, and oxidized form is reduced to reduced form.
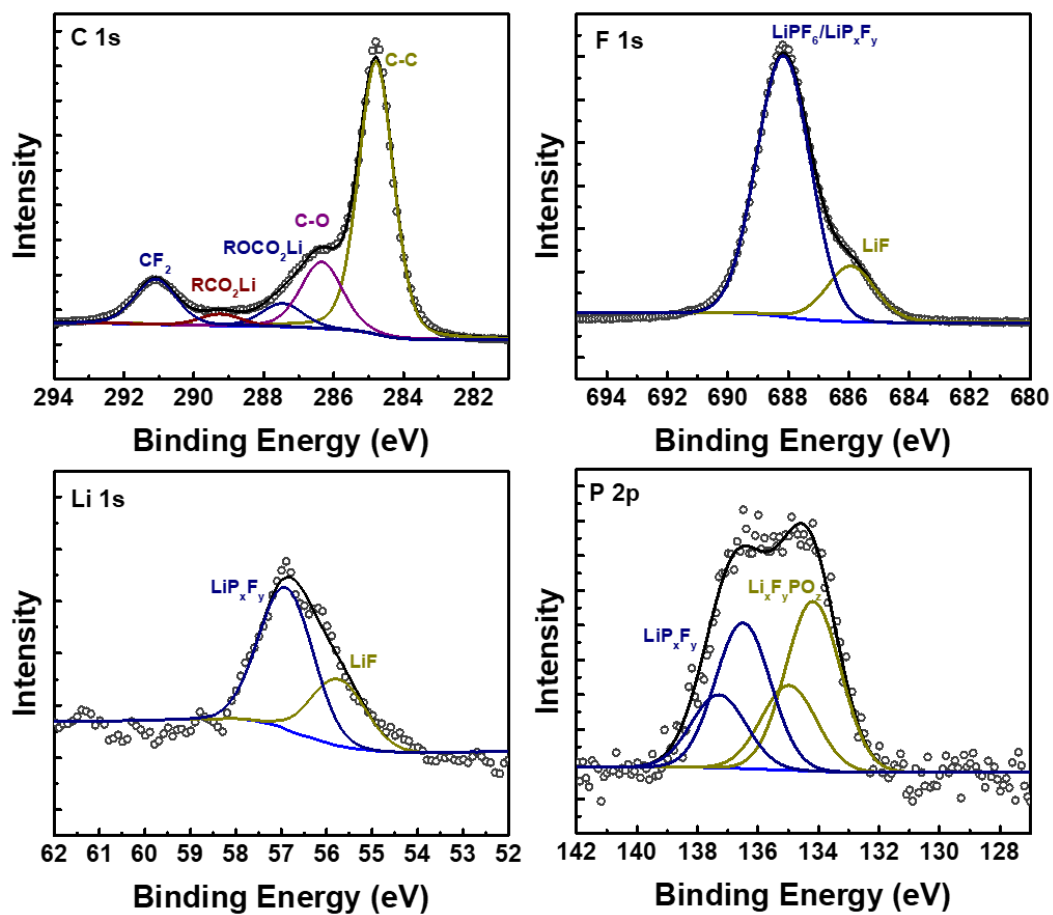
Figure S9. XPS results of different elements on the NMC811 cathode surface after charged to 4.3 V (Vs Li/Li+) in LiPF6/PC electrolyte.
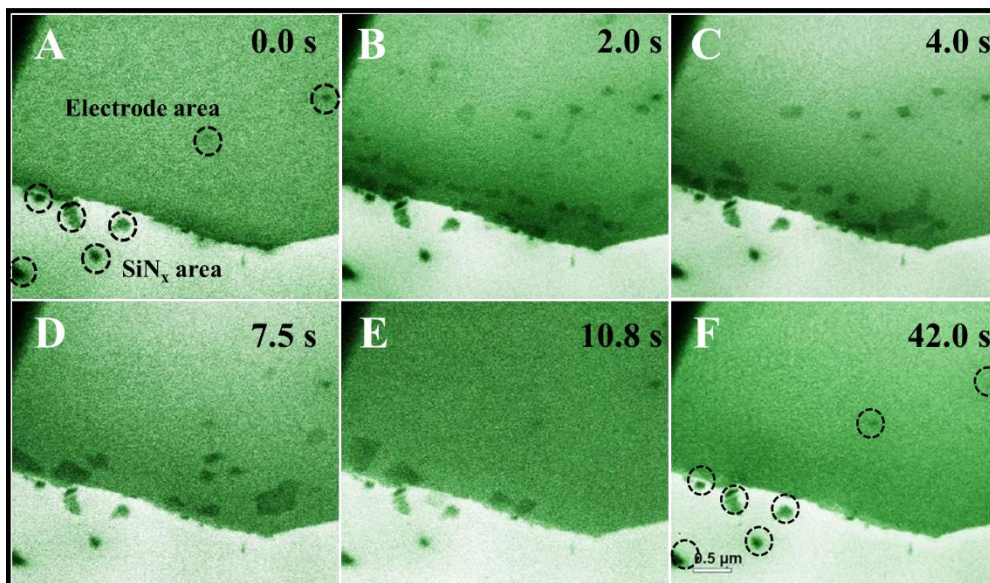
Figure S10. Time series of TEM images illustrate formation of LiF nanosheets on Ti electrode and the nanosheets movement on Ti electrode in Movie S2 [7 dark spots marked with black circles are unchanged (unreacted) dark spots], which are corresponding to images in Figure 3A - F.
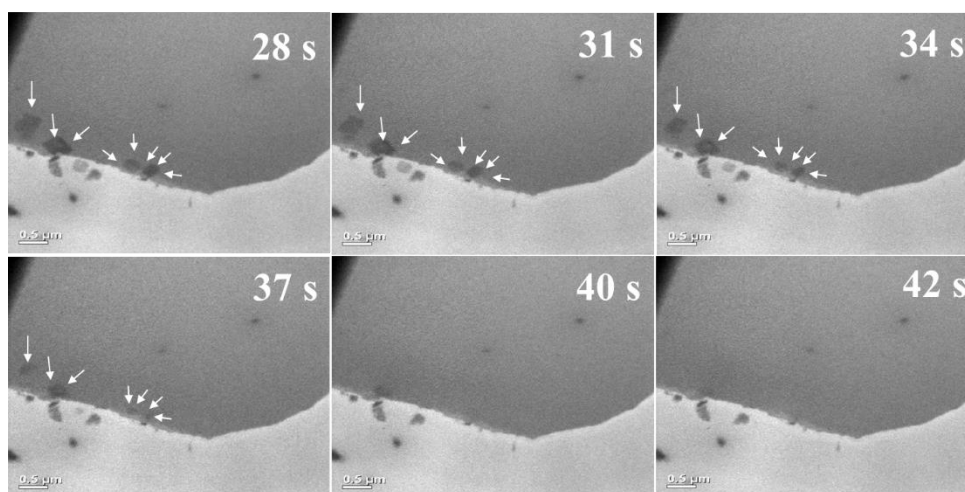

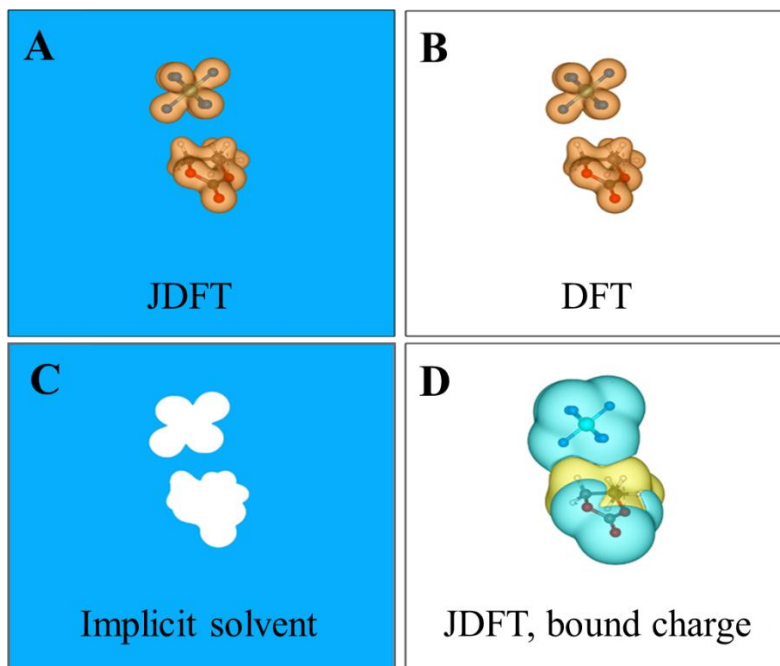**Figure S11**.Dissolution of LiF nanosheets under negative current in Movie S2.

Figure S12. JDFT simulation of PC+PF$_6^-$. The configuration is the same with that in **Figure 4AIII**.

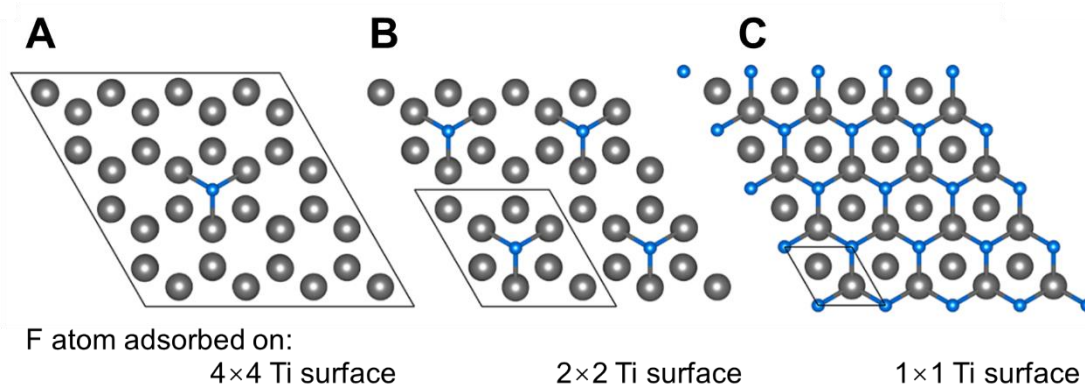
F atom adsorbed on:
4×4 Ti surface   2×2 Ti surface   1×1 Ti surface

Figure S13. Top view of fluorinated Ti (0001) surface.